High-Fidelity Particle-In-Cell Simulations of Ion Thruster Optics

IEPC-2017-451

Presented at the 35th International Electric Propulsion Conference
Georgia Institute of Technology – Atlanta, Georgia – USA
October 8–12, 2017

Tilman Binder*, Marcel Pfeiffer†, and Stefanos Fasoulas‡
Institute of Space Systems (IRS), University of Stuttgart, Stuttgart, 70569, Germany

and

Hans Leiter§
ArianeGroup GmbH, Lampoldshausen, 74239, Germany

The numerical simulation of ion thruster optics is one of the most common applications of particle-based methods in the field of electric propulsion. Over the years, powerful tools for simulation of ion trajectories and charge exchange erosion have been developed and validated. The validity of prediction results is high as long as the ion optics system is operated far from the electron back-streaming (EBS) limit. Operating gridded ion thrusters with EBS is one of the most dangerous failure modes, a fully kinetic numerical modeling is therefore highly desirable. For this, a more sophisticated approach based on high fidelity Particle-In-Cell (PIC) methods is expected to be necessary, capable to realistically handle the different scales of heavy ions and very low mass electrons. In this paper, electrostatic optics simulations of a RIT-μX thruster are conducted. The results are compared with simulations assuming the common Boltzmann relation. The spatial distributions of electric potential and number densities as well as the determined back-streaming currents match well. The velocity distribution functions of electrons correspond at most positions to thermal equilibrium. The comparison between simulations of the actual thruster and a corresponding infinite pattern of grid apertures show that the state at edge apertures differs only slightly. The experimentally determined EBS threshold, however, could not be reproduced, which is probably caused by various assumptions made for the simulation parameters.

Nomenclature

BC	= boundary condition	F	= source term	ref	= reference
BR	= Boltzmann relation	I_{beam}	= beam current	t	= time
EBS	= electron back-streaming	k_B	= Boltzmann constant	T	= temperature
FK	= fully kinetic	m	= (particle) mass	$\mathbf{v}$	= velocity
HDG	= Hybrid Discontinuous Galerkin	n	= number density	w_k	= weighting factor
VDF	= velocity distribution function	N_{cells}	= number of cells	$\mathbf{x}$	= position
e, e^-	= electron	$N_{\mathcal{O}}$	= spatial order	ρ	= charge density
f	= particle distribution function	q	= (particle) charge	Φ	= potential, voltage

*Ph.D. Student, Institute of Space Systems (IRS), binder@irs.uni-stuttgart.de.
†Postdoctoral Researcher, Institute of Space Systems (IRS), mpfeiffer@irs.uni-stuttgart.de.
‡Head of Institute, Institute of Space Systems (IRS), fasoulas@irs.uni-stuttgart.de.
§Team Leader Electric Propulsion, ArianeGroup GmbH, hans.leiter@ariane.group.

I. Introduction

NUMERICAL simulations have gained a lot in importance for engineering during the last decades. Today, they can be seen as crucial complement to experiments and give insight into complex physical phenomena. In the field of electric propulsion, the simulation of ion thruster optics is seen as one of the most mature applications of numerical simulation.[1] Over the years, a large number of powerful tools for the simulation of ion trajectories and charge exchange erosion have been developed. The high validity of prediction results of even strongly simplified simulation methods might suggest that there are no new topics to investigate in this field, especially for high-fidelity codes. However, not fully conservative physical models such as steady-state flux tubes[2] or retroactive enforcement of energy conservation[3,4] have to be applied with caution. These simplifications are likely to fail when a kinetic modeling of both ions and electrons is relevant, which is mostly the case when electron fluid models such as the Boltzmann relation (BR) lose their validity. This applies when the electrons are, for instance, part of a non-isothermal expansion or even not in thermodynamic equilibrium at all, or when they have passed across a minimum potential barrier and their drift velocity cannot be neglected. The latter occurs when ion optics systems are simulated at operation near or beyond the electron back-streaming (EBS) limit, as will be shown later in this paper.

Thruster qualification regarding EBS, as one of the most dangerous failure modes for ion thrusters, is conducted mostly experimentally, but in a simplified way also numerically based on BR.[5] A fully kinetic numerical modeling of this topic would give important new insight, in terms of investigating the actual limits of simplified approaches and creating baseline cases for more sophisticated models. However, highly parallel computation concepts are necessary to attain feasible simulation times when handling the different scales of heavy ions and very low mass electrons and additionally for the relatively large geometries when considering more than a single beamlet. This problem is tackled by applying the Hybrid Discontinuous Galerkin Poisson solver of the 3D PIC-DSMC code PICLas.[6]

Fully kinetic (FK) ion optics simulations published in the past showed a significant deviation of electron densities in the neutralizing region of the beam compared to results assuming BR electrons, which the authors stated to be linked to non-Maxwellian velocity distributions of electrons.[7] Therefore, we would also like to address these differences by comparing FK with BR results considering both electron densities and velocity distributions.

Besides investigating the limits of BR, in this case for EBS estimation, the simulations can be also seen as preparatory step for detailed analyses of beam neutralization near the ion optics, since corresponding previous studies focused rather on the total resulting beam instead of individual beamlets.

The paper is structured as follows. First, the theory behind the kinetic modeling of plasma flows and the Particle-In-Cell (PIC) method is introduced briefly. Next, the set-up of the simulations is defined and afterwards the results are presented and discussed. The simulation result for the actual thruster geometry, a RIT-μX of Airbus, is compared with a corresponding infinite pattern of grid apertures. For the latter case, the ion optics were simulated with different accel grid voltages at constant beam currents. The development of the predicted back-streaming currents is compared with EBS measurements conducted by Airbus.

II. Theory

The kinetic behavior of a plasma consisting of individual particles (i.e., ions, electrons, and neutral gas) can be described by the Boltzmann equation:

$$\frac{\partial f_\alpha}{\partial t} + \mathbf{v}_\alpha \frac{\partial f_\alpha}{\partial \mathbf{x}_\alpha} + \frac{\mathbf{F}}{m_\alpha} \frac{\partial f_\alpha}{\partial \mathbf{v}_\alpha} = \left(\frac{\delta f}{\delta t}\right)_{Coll} \tag{1}$$

Here, $f_\alpha = f_\alpha(\mathbf{x}, \mathbf{v}, t)$ is the particle distribution function of the particle species α depending on position $\mathbf{x}$, velocity $\mathbf{v}$, and time t. In addition, m is the particle mass, and $\mathbf{F}$ is the Lorentz force which is given in the electrostatic case by

$$\mathbf{F} = q_\alpha \mathbf{E} \tag{2}$$

$$\Delta\Phi = -\frac{\rho}{\epsilon_0} \tag{3}$$

$$\mathbf{E} = -\nabla\Phi \tag{4}$$

with the particle charge q, the electric field $\mathbf{E}$, the electrostatic potential Φ, and the vacuum permittivity ϵ_0.

By the kinetic approach, the charge density ρ is defined as

$$\rho(\mathbf{x},t) = q\int_{\mathbb{R}^3} f(\mathbf{x},\mathbf{v},t)\mathrm{d}^3v. \tag{5}$$

The used PICLas code[6] models the relation between $\mathbf{E}$ and ρ numerically by the well-known PIC method.[8] The collision term $(^{\delta f}/_{\delta t})_{Coll}$ describes binary collisions including chemical reactions and can be considered by approaches such as Direct Simulation Monte Carlo (DSMC)[9] or Monte Carlo Collisions (MCC).[10] The particle distribution function is approximated as the linear combination of N_p individual δ-functions with a weighting factor w_k:

$$f(\mathbf{x},\mathbf{v},t) \approx \sum_{k=1}^{N_p} w_k \delta\left(\mathbf{x}-\mathbf{x}_k(t)\right)\delta\left(\mathbf{v}-\mathbf{v}_k(t)\right). \tag{6}$$

This approximation can be taken as N_p particles at positions $\mathbf{x}_k$ with velocities $\mathbf{v}_k$ and particle weights w_k. In other words, the plasma is modeled by a certain amount of representative particles which are tracked through the computational domain and react to the forces based on self-consistent fields resulting from the Poisson equation (Eq. (3)) with the applied voltages as boundary conditions.

A. Boltzmann relation

The Poisson equation is changed for the assumption of the Boltzmann relation (BR). The BR is a very common fluid approximation[11] for the electron density assuming that the electron fluid is isothermal, its pressure follows an ideal gas behaviour, and that the drift velocity of electrons can be neglected. The advantage of electron fluid models such as BR is that they eliminate the different particle time scales between ions and electrons. For the BR, the electron number density n_e is given by

$$n_e^{BR} = n_{e,ref}\cdot e^{q_e(\Phi-\Phi_{ref})/k_B T_e} \tag{7}$$

with the electron temperature T_e, the potential Φ at the location of n_e, electron charge q_e, Boltzmann constant k_B, and a reference Φ_{ref} at the location of $n_e = n_{e,ref}$. Thus, Eq. (3) is extended to the non-linear source term of

$$\rho(\Phi) = \rho_{ion} + q_e n_e^{BR}(\Phi). \tag{8}$$

The definition of the reference with Φ_{ref} and $n_{e,ref}$ is mostly based on a quasi-neutrality assumption at a known location with $n_e = n_{ion}$. The exponential dependency $\rho_e(\Phi) \propto e^{q_e\Phi/k_B T}$ can be numerically problematic due to floating point overflows where $\Phi > \Phi_{ref}$. Therefore, it can be beneficial to use the linear approximation in this regime:

$$e^{q_e\Phi/k_B T} \approx 1 + q_e\Phi/k_B T \tag{9}$$

However, the reference then has to be shifted above the maximum expected Φ of the converged solution to ensure physically correct results.

B. The PIC method and field solver

For reasons of computational costs of particle tracking as well as parallel efficiency, a moderate number of mesh cells is desirable. To fulfill this demand, a high order method for solving the Poisson equation is necessary to additionally overcome the resolution requirements to correctly resolve the physical effects. In PICLas, this is enabled by the Hybrid Discontinuous Galerkin (HDG) method, which is both cell-local and inherently allows high-order spatial discretization.

In the PIC method, the particle information is "deposited" onto interpolation points that are fixed within the simulation domain. To consistently sustain the high order approach, this interpolation is done with a higher order shape function instead of simple linear interpolation. With this information, the source term F for the field solver is determined. In the next step, the resulting field is solved on the interpolation points using the HDG method. Here, the Poisson equation with the electric potential Φ is reformulated as

$$\Delta\Phi = -F \quad \rightarrow \quad \mathbf{u} = -\nabla\Phi\ , \quad \nabla\mathbf{u} = F \tag{10}$$

using the introduced gradient variable $\mathbf{u}$ as additional unknown variable besides Φ. This resultant mixed form is solved in a DG-SEM framework[12] using the algorithm described by Cockburn et al.[13] with a conjugate

gradients method (CG). For this, a third unknown variable λ is introduced as the unique solution of Φ existing (together with $\mathbf{u}$) on the cell-sides only and with further requirements on the numerical flux. The idea of the introduced λ is the reduction of the total system size. In a classic 3D-DG frame of spatial order $N_\mathcal{O}$ with a number of N_{cells} cells, the total number of degrees of freedom (DOF) in the system is $N_{cells}(N_\mathcal{O}+1)^3$. In the HDG method the solution exists on the cell-sides. If each cell has 3 unique sides (the other 3 sides correspond to the neighboring cell, except boundary sides), the total number of DOF is $3N_{cells}(N_\mathcal{O}+1)^2$. Therefore, the system size is reduced with HDG for $N_\mathcal{O} > 2$.

The solution needs to be changed if the Boltzmann relation (Eq. (8)) is used for electrons with the source term depending on the potential itself:

$$\Delta\Phi = -F(\Phi) = -\frac{1}{\varepsilon_0}\left(\rho_{ion} + \rho_e(\Phi)\right). \tag{11}$$

Here, ρ_{ion} is still the ion charge density from the particle interpolation step. To solve this non-linear equation the root finding process of the residuum R has to be performed:

$$R(\Phi) = \Delta\Phi + F(\Phi) \stackrel{!}{=} 0, \tag{12}$$

which is realized by a Newton method:

$$R(\Phi^i) + \left.\frac{\partial R}{\partial \Phi}\right|_{\Phi^i} \delta\Phi = 0 \tag{13}$$

$$\Phi^{i+1} = \Phi^i + \delta\Phi\ , \quad i = 0, 1, .. \tag{14}$$

This iteration calls the CG solver in each step and is repeated until $\|R(\Phi^{i+1}) - R(\Phi^i)\| < \epsilon$ with a defined accuracy ϵ.

III. Simulation Set-up

Two different geometries were considered - the actual complete thruster and the corresponding, effectively infinite pattern of apertures. Fig. 1 depicts the thruster together with the two simulation domains. The discharge chamber of 40 mm diameter is closed by a two-grid system with 37 apertures in a pattern within a diameter of approximately 20 mm. A diverging ring follows behind the grids. The simulation domain (shown in red) is reduced by symmetry conditions to a 30° piece and the upstream sections are restricted to distances from the apertures beyond which they do not influence the solution. For the infinite pattern (shown in blue), the symmetry conditions reduce the topology to two quarter apertures. Fig. 2 depicts the surface meshes and applied boundary conditions (BCs). Parts of the frontal symmetry BC are cut away for vizualizing the hidden sides. The distance from inflow plane to the upstream edge of the accel grid ($x = 0$) is 1 mm and the further distance to the outflow plane is 17 mm. The number of mesh cells is 90758 and 5488, respectively. A polynomial degree of $N_\mathcal{O} = 4$ was used, i.e., each cell contains $5 \cdot 5 \cdot 5 = 125$ interpolation points by which the actual spatial discretization needs to be taken as being much finer. The simulation parameters and BCs are summarized in Tab. 1. The potential difference between inflow and screen grid corresponds to an assumed plasma potential of 15 V and the voltage of the acceleration grid was varied for the different simulations.

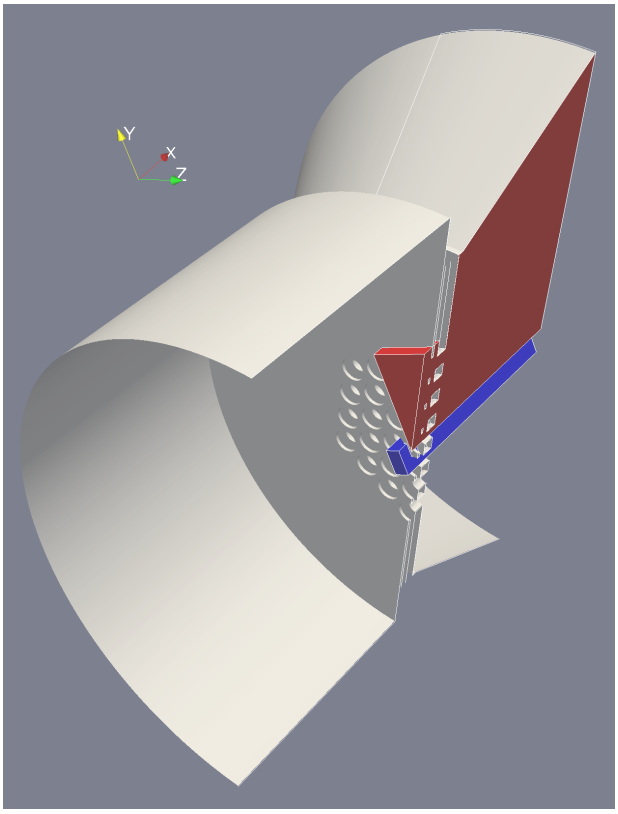

Figure 1: Simulation domains and half thruster.

The upstream plasma density as inflow BC was iterated for each case so that the resulting total beam current matches $I_{beam} = 6\,\mathrm{mA}$ when used for the complete thruster simulation. Open BCs remove crossing particles from the simulation, for solid boundaries this assumes a recombination to neutral species, which are not considered afterwards. The temporal integration of particle trajectories was performed by a 5-stage, low-storage, explicit Runge-Kutta scheme of 4^{th} order with different time steps for FK and BR simulations (cf. Tab. 1b). The axial position $x_{\Phi,min}$ of the minimum potential near the acceleration grid was estimated by preparatory simulations. BR-electrons corresponding to the inflow BC were included for $x < x_{\Phi,min}$, and to the outflow BC for $x > x_{\Phi,min}$. For infinite pattern simulations, the average ion density at the outflow plane was taken as reference resulting in an electron number density of approximately $4.4 \cdot 10^{15}\,\mathrm{m}^{-3}$. For fully kinetic, complete thruster simulations, the value was determined adaptively, based on the averaged ion-densities inside the boundary-adjacent cells. Thus, both upstream and downstream states are taken as quasi-neutral plasma. To eliminate the (statistical) influence of kinetic electrons originating from the inflow BC on the solution, the upstream region of BR-electrons was also assumed in FK simulations, i.e., fully kinetic electrons are coming only from the outflow BC. This is justified by the already determined equality of BR- and kinetic electrons in the upstream region of ion optics simulations,[7] but it was additionally verified by ourselves. FK simulations were continuations from BR simulations, since this allows to take an already fully expanded ion beam as initial condition and the time for reaching steady state is decreased significantly. Before the first time step of these continuation simulations, kinetic electrons were sampled in the downstream BR-region once, corresponding to the cell-average number density from Eq. (7) and a Maxwellian velocity distribution with the electron temperature. Steady state was assumed based on the total particle number and convergence of the shown quantitative simulation results, which was typically the case after a few μs simulated time.

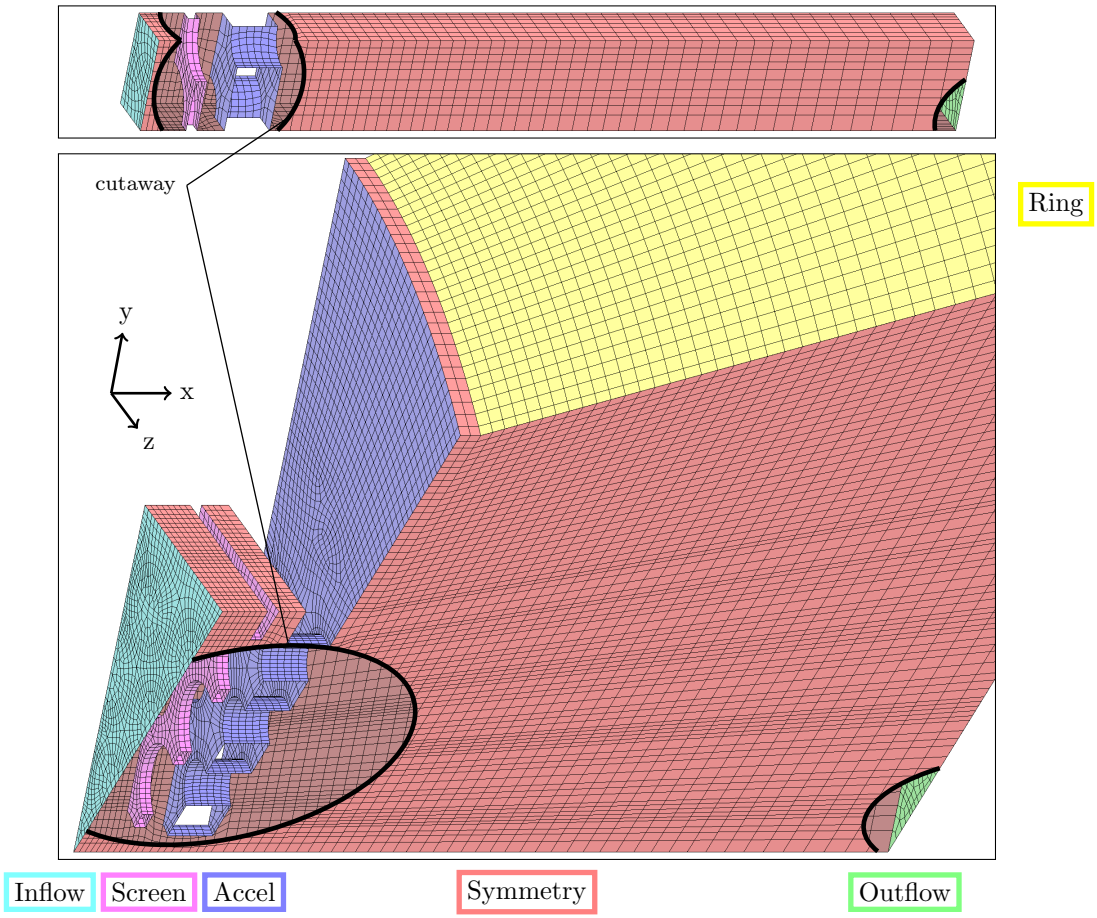

Figure 2: Used computational (surface) meshes and boundary conditions.

Name	Field-BC	Particle-BC
Inflow	$\Phi = 1565\,\mathrm{V}$	open, Xe^+ emitting
Screen	$\Phi = 1550\,\mathrm{V}$	open
Accel	$\Phi = \Phi_{accel}$	open
Symmetry	$\frac{\partial \Phi}{\partial \mathbf{n}} = 0$	reflective
Outflow	$\Phi = 0\,\mathrm{V}$	open, e^- emitting
Ring	$\Phi = 0\,\mathrm{V}$	open

(a) Boundary conditions.

Spatial order	$\mathcal{O}(4)$
Temporal order	$\mathcal{O}(4)$
Time-step FK	$\Delta t_{FK} = 5 \cdot 10^{-11}\,\mathrm{s}$
Time-step BR	$\Delta t_{BR} = 5 \cdot 10^{-9}\,\mathrm{s}$
Simulation particle weight	$w_k \approx 550$
Inflow-Xe^+ number density	$n_{Xe^+} \approx 1.1 \cdot 10^{17}\,\mathrm{m}^{-3}$
Inflow-Xe^+ velocity	$v_{Xe^+} = 2500\,\mathrm{m/s}$
Inflow-Xe^+ temperature	$T_{Xe^+} = 450\,\mathrm{K}$
Inflow-e^- temperature	$T_{e^-}^{in} = 3.5\,\mathrm{eV}$
Outflow-e^- temperature	$T_{e^-}^{out} = 2\,\mathrm{eV}$

(b) Simulation parameters.

Table 1: Simulation set-up.

IV. Results

A. Infinite aperture pattern

The voltage of the acceleration grid Φ_{accel} was successively decreased until significant EBS occured. Before we quantify the predicted EBS, the simulation results are evaluated in terms of comparing BR with FK. The chosen figure of merits are the spatial distributions of number densities and electric potentials. To reduce the statistical noise of the PIC method, the values were averaged for several thousand time-steps during steady state and are an evaluation of the DG-polynomial on an equidistant visualization mesh. The number densities access the source term from Eq. (11), based on high order Gaussian shape functions with boundary-dependent corrections[a]. Figures 8 and 9 in the appendix show the line plots along the axis through a beamlet and Figs. 10 and 11 equidistantly between the beamlets, intersecting the screen and accel grid (which are depicted by the shaded areas). Basically, the curves of the potential Φ (black), ion number density n_{Xe^+} (blue), and electron number density n_{e^-} (green and downstream part of the red line) need to be compared. It can be seen that the FK simulations (solid lines) match the BR ones (dashed lines) well. For decreasing Φ_{accel} the deviation increases, but it remains small. This deviation is strongly linked to the state at $x_{\Phi,min}$: If the corresponding potential is significantly lower than at the outflow plane (i.e., $\ll 0\,\mathrm{V}$), the density of BR electrons drops toward zero, as it is also the case for kinetic electrons. In this case, the increasing potential in upstream direction at $x < x_{\Phi,min}$ is insignificant, since no electrons pass the barrier, which motivates the assumption of confined BR regions as described in the previous section. Otherwise, the BR would predict a likewise increasing n_{e^-}. For an accel grid voltage at the EBS limit, electrons pass the barrier (cf. Fig. 9). In contrast to the BR, however, the electron density does not increase, since they are strongly accelerated towards the upstream direction so that the electron drift velocity can not be neglected anymore. For these cases, the simulated number density of electrons deviates approximately with one order of magnitude at $x_{\Phi,min}$. At positions between the beamlets (Figs. 11 and 10), the potential is always monotonically decreasing towards the accel grid, due to which the deviation between FK and BR is insignificant.

One peculiarity of the shown line plots is the case of the most positive voltage, $\Phi_{accel} = -100\,\mathrm{V}$, which is augmented even more for further increased voltages (which are not included in this paper). It was found that this is associated rather with limitations of the boundary conditions instead of a real physical background. If the kinetic electrons are not in thermodynamic equilibrium even near their inflow BC, they can not be expected to follow the BR predictions. The velocity distribution function (VDF) is a Maxwellian in the equilibrium case. Also in the simulated plasma, electrons oscillate around ions. In an averaged homogeneous state, this means that through an arbitrary section inside the domain the same amount of electrons pass

[a]These corrections consider respective multiple mirrorings at symmetry planes, particle sampling from assumed homogeneous distributions outside of the simulation domain, and continuation from outflowing particles.

through one direction as through the opposite one, each with the respective half-Maxwellian VDF. When relatively strong fields exist at the BC, however, this half-Maxwellian is shifted and does not complement the equilibrium phase space anymore.

During the same averaging phases of the spatial distributions, there were also the individual particle velocities inside defined volumes stored for evaluating the VDF. For checking spatial homogeneity inside these volumes, the resulting histograms are shown for three different reference volumes x_{min}, x_{max}, and y_{min}, which are illustrated in Fig. 3.

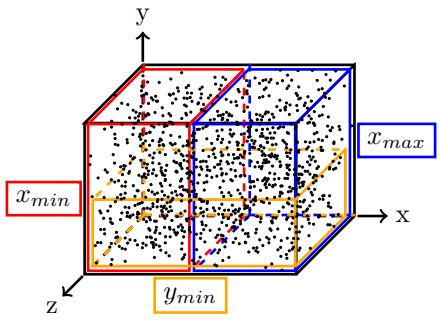

Figure 3: Reference volumes for histograms.

Figures 12–17 in the appendix depict the VDF with decreasing x, both at positions along the axis through the beamlets and equidistantly between them. The color of the markers corresponds to the reference volume in Fig. 3. The histograms are shown together with the equilibrium VDF of the specified electron temperature. Figures 12 and 13 show the distributions close to the inflow BC for kinetic electrons ("Outflow" in Fig. 2). It can be seen that the defined electron temperature of $T_{e^-}^{out} = 2\,\mathrm{eV}$ is sustained for nearly all grid voltages. Only for the mentioned case of $-100\,\mathrm{V}$, a higher temperature follows with additional deviations from equilibrium in terms of more small negative v_x between the beamlets (cf. Fig. 13b). For further upstream positions, the temperature deviates slightly from 2 eV at the axis; there are strong deviations for the $-100\,\mathrm{V}$ case. Between the beamlets, the electrons are in perfect equilibrium and isothermal which is also in accordance with the matching results of FK and BR for potential and number densities. Figure 16 depicts the VDF at $x_{\Phi,min}$ where significant electrons exist only for $\Phi_{accel} > -130\,\mathrm{V}$. The reference volume includes the entire radial extent, therefore, the histograms of the y_{min}-volume are not shown. Both the $-130\,\mathrm{V}$ and the $-120\,\mathrm{V}$ case are in thermal equilibrium for v_y. In axial direction, the following strong acceleration is visible. Electrons pass towards the negative direction but are further accelerated afterwards so that none oscillate back. Additionally, the number of particles with small negative velocities is reduced which leads to a larger directed mean velocity. At the most upstream position (Fig. 17), where the strong potential gradient between both grids exists, the axial drift velocity of more than $1 \cdot 10^7\,\mathrm{m/s}$ into negative direction is now eminent. The ongoing acceleration explains the spatial inhomogeneity that also distorts the depicted VDF.

In summary, the spatial distributions of Φ and n match well between FK and BR simulations. This is confirmed by the fact that also the VDF corresponds at most positions to thermal equilibrium. The largest differences exist inside the beamlet at $x \leq x_{\Phi,min}$. The more profound deviations for the most positive accel grid voltage, however, are expected to be associated with perturbed boundary conditions.

B. Actual thruster

The full thruster geometry was simulated with fully kinetic electrons for an accel grid voltage of $-120\,\mathrm{V}$. Figure 4 depicts a contour plot of ion and electron number densities (the extracted plane is the frontal symmetry plane in Fig. 2). It can be seen that the individual beamlets are nearly identical. Only the most outer beamlet deviates slightly, because it is influenced by the low voltage of ring and outer accel grid. The different locations are also compared between each other in Figs. 5 and 6 together with the results from the corresponding infinite pattern. The first depicts an inner and outer beamlet axis, whereas the second shows the inner and outer centerline between beamlets. It can be seen that the deviations are very small indeed. Please note that the averaging time for the thruster simulation was shorter than for infinite pattern simulations which results in increased statistical noise.

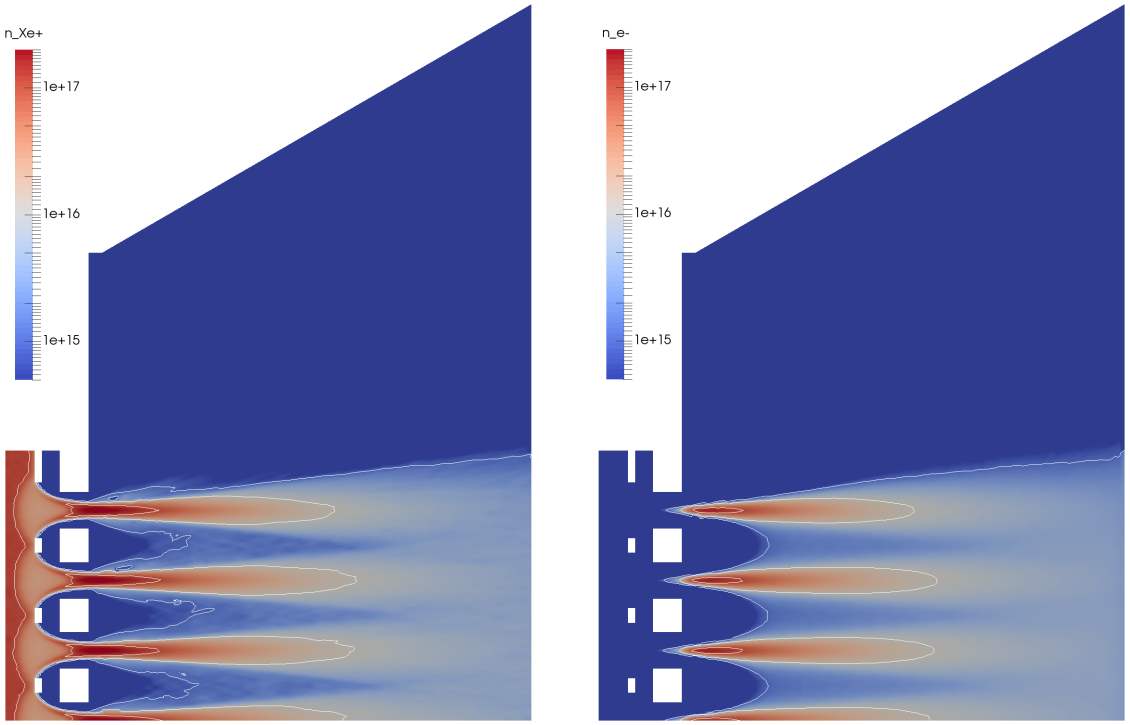

Figure 4: Contour plot of plane through thruster at $\Phi_{accel} = -120\,\mathrm{V}$ (left: n_{Xe^+}, right: n_{e^-}, both in m^{-3}).

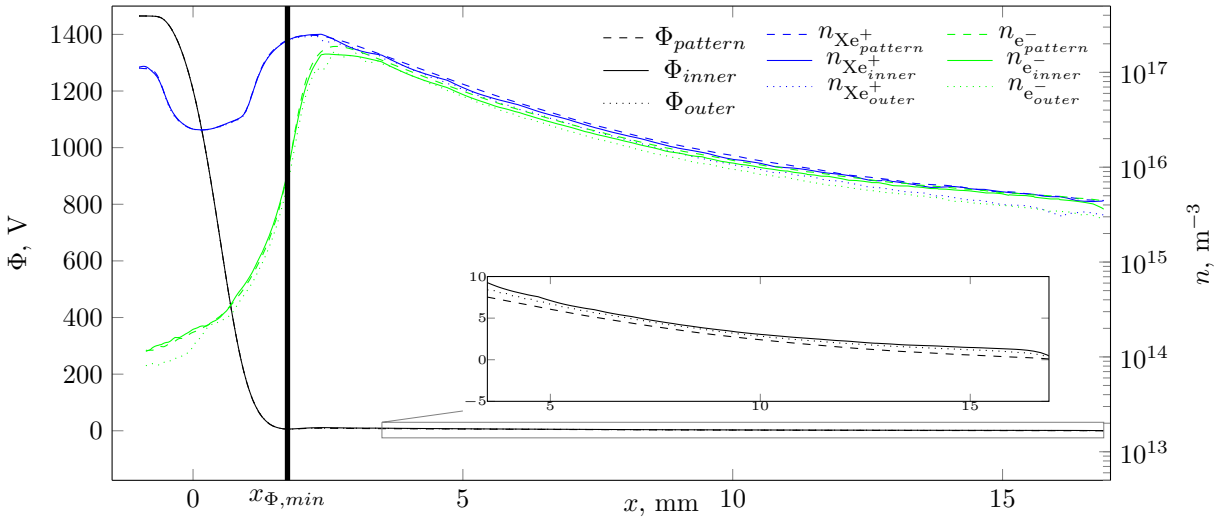

Figure 5: Axis plots through beamlets for thruster and infinite pattern.

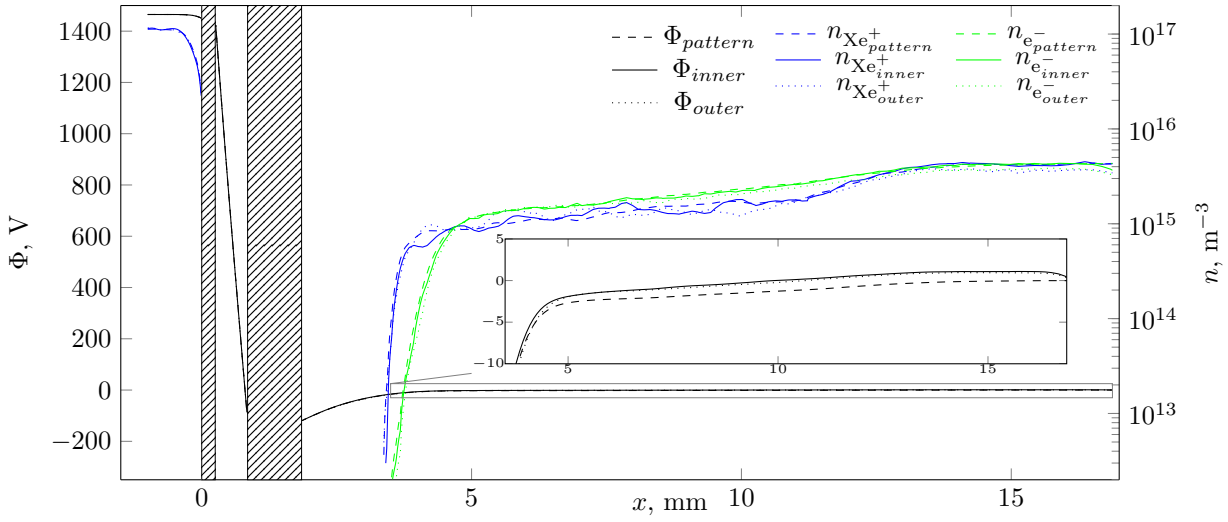

Figure 6: Center plots between beamlets for thruster and infinite pattern.

C. Quantitative EBS evaluation

Having both FK and BR simulations, the actual back-streaming electron current can be calculated by two methods. First, for FK electrons, the particles crossing the upstream BC simply have to be counted. Secondly, for BR electrons, the thermal flux at $x = x_{\Phi,min}$ needs to be integrated.[5] The resulting values are summarized in Tab. 2 scaled with the beam current. It can be seen that BR and FK simulations also match very well for these results. Since the flux is proportional to number density and directed mean velocity, the observed lower number densities at $x_{\Phi,min}$ for FK cases (cf. Fig. 9) are exactly compensated by the larger velocities. This agrees also with the described VDF (cf. Fig. 16). With respect to the comparison between simulations of infinite pattern and full thruster, Tab. 2 shows that that difference is very small as well. Additionally, it was found that the maximum deviation in electron current between the individual beamlets of the thruster is around 20 %, slightly decreasing outwards.

Φ_{accel}	-300 V	-150 V	-140 V	-130 V	-120 V	-100 V
$I_{EBS,BR}/I_{beam}$	$1.01 \cdot 10^{-35}$	$1.40 \cdot 10^{-6}$	$9.25 \cdot 10^{-5}$	$4.95 \cdot 10^{-3}$	$9.54 \cdot 10^{-2}$	$6.45 \cdot 10^{-1}$
$I_{EBS,FK}^{inf.pattern}/I_{beam}$	-	-	$6 \cdot 10^{-5}$	$4.0 \cdot 10^{-3}$	$9.7 \cdot 10^{-2}$	$6.82 \cdot 10^{-1}$
$I_{EBS,FK}^{thruster}/I_{beam}$	-	-	-	-	$9.5 \cdot 10^{-2}$	-

Table 2: Simulated back-streaming electron currents.

The simulated current ratios are plotted in Fig. 7, together with an experimental EBS evaluation based on power consumption for $I_{beam} = 6$ mA. The measurements indicate an EBS threshold around $\Phi_{accel}^{EBS} = -80$ V. The simulations, however, show that significant EBS already starts around -120 V. Besides experimental uncertainties, this difference is expected to be caused by various assumptions made for the simulation parameters such as the upstream plasma state and electron temperature. A next step will be a sensitivity analysis with regard to these values. Furthermore, the actual neutralization process of the plume was not considered in the simulations, since the quasi-neutrality was simply assumed. Future simulations will focus on this topic.

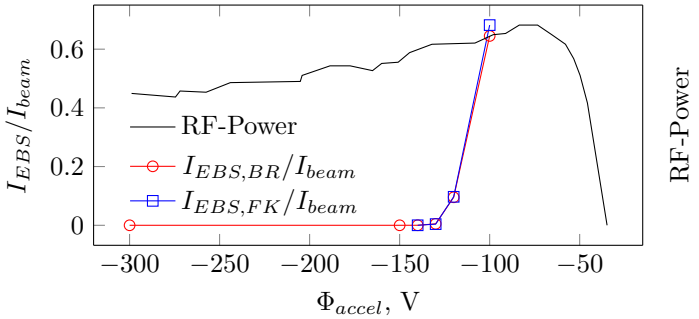

Figure 7: Comparison of EBS thresholds.

Appendix

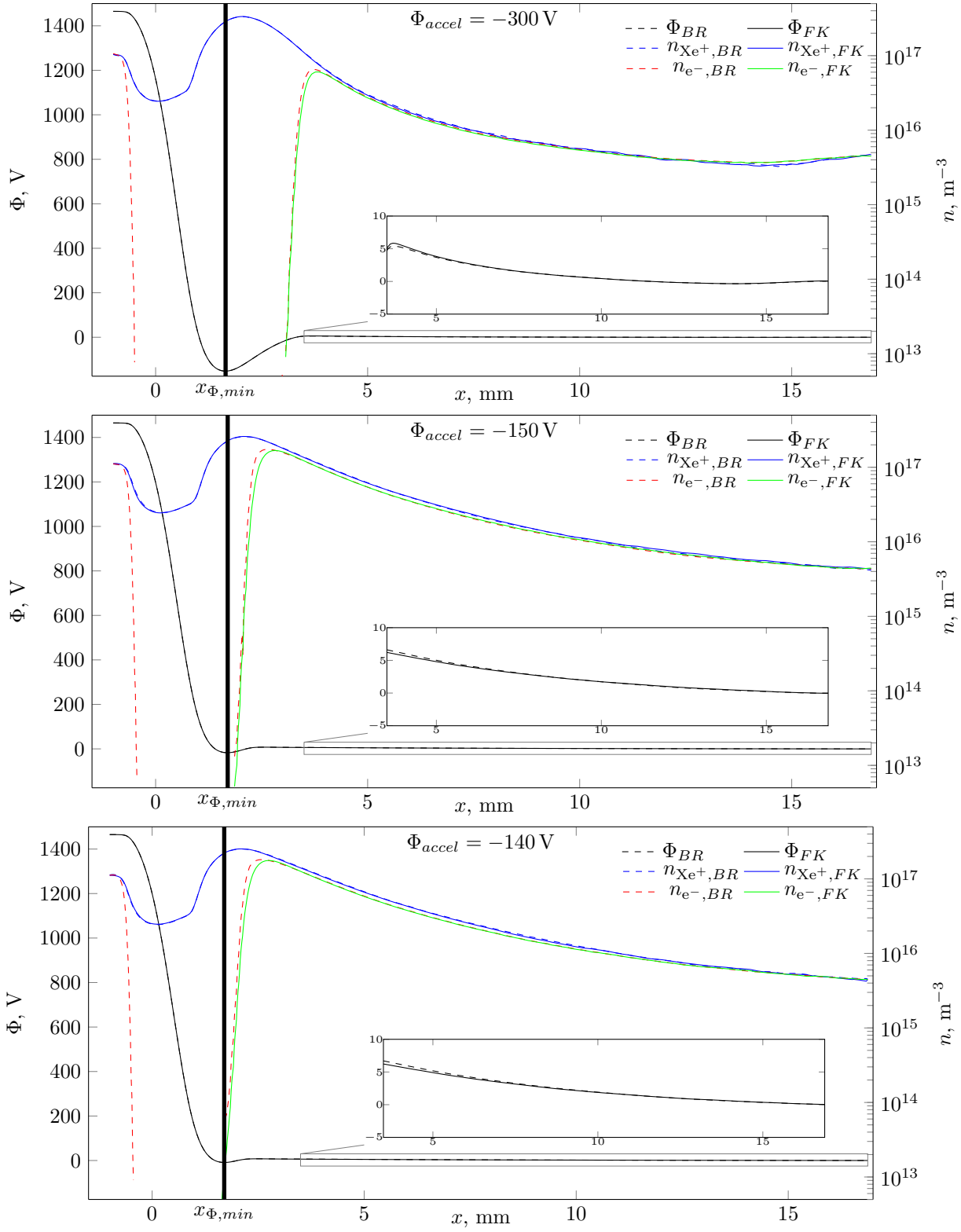

Figure 8: Axis plots through beamlets of infinite pattern for $\Phi_{accel} = -300\,\mathrm{V}$ to $-140\,\mathrm{V}$.

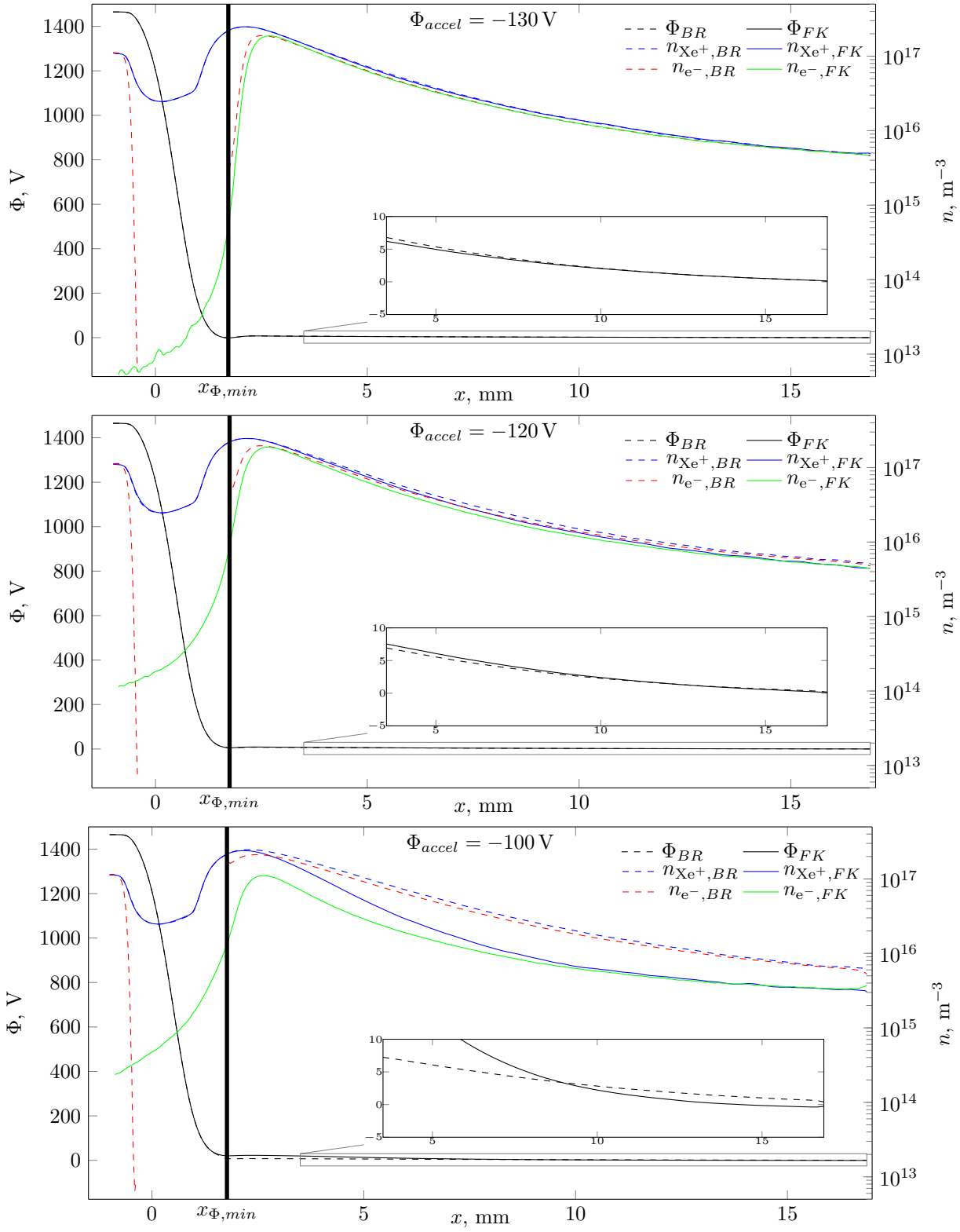

Figure 9: Axis plots through beamlets of infinite pattern for $\Phi_{accel} = -130\,\mathrm{V}$ to $-100\,\mathrm{V}$.

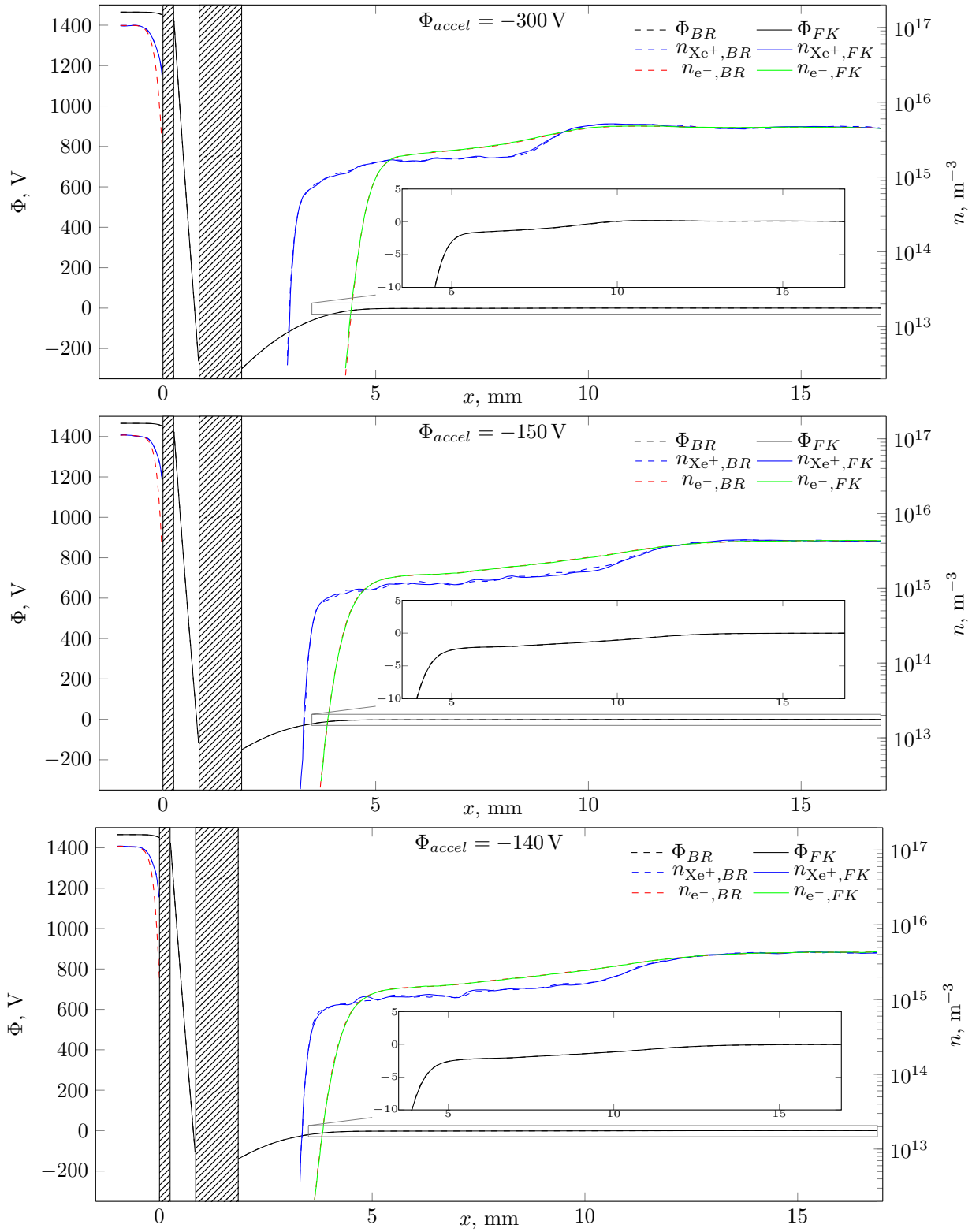

Figure 10: Center plots between beamlets of infinite pattern for $\Phi_{accel} = -300\,\mathrm{V}$ to $-140\,\mathrm{V}$.

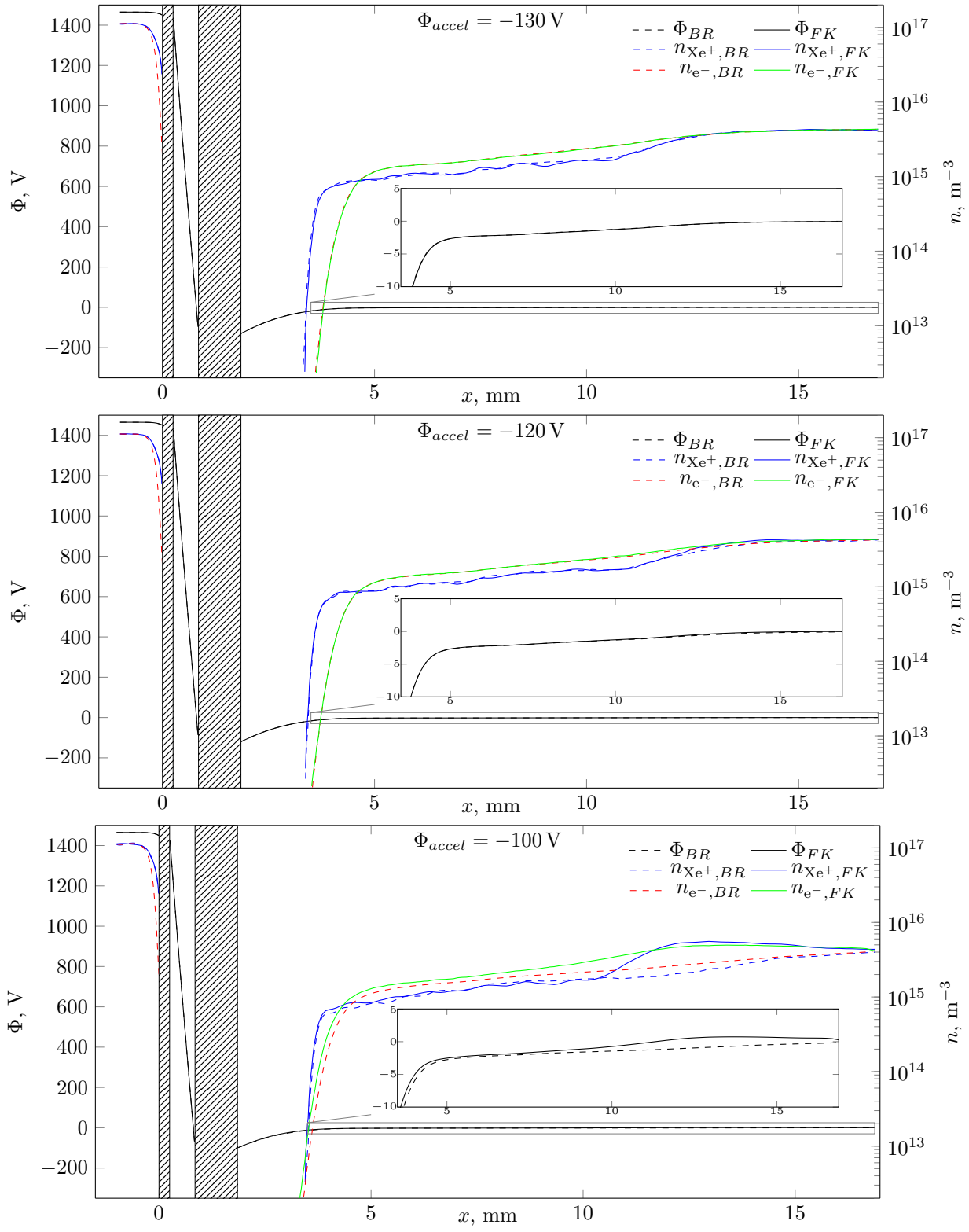

Figure 11: Center plots between beamlets of infinite pattern for $\Phi_{accel} = -130\,\mathrm{V}$ to $-100\,\mathrm{V}$.

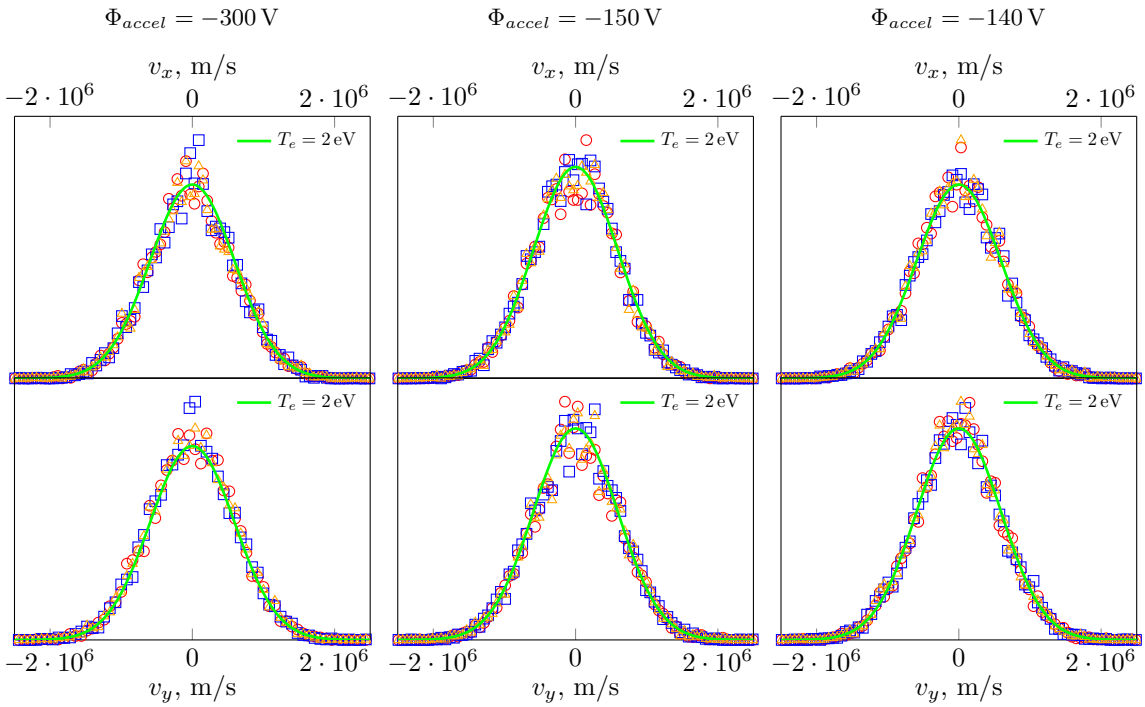

(a) $\Phi_{accel} = -300\,\mathrm{V}$ to $-140\,\mathrm{V}$.

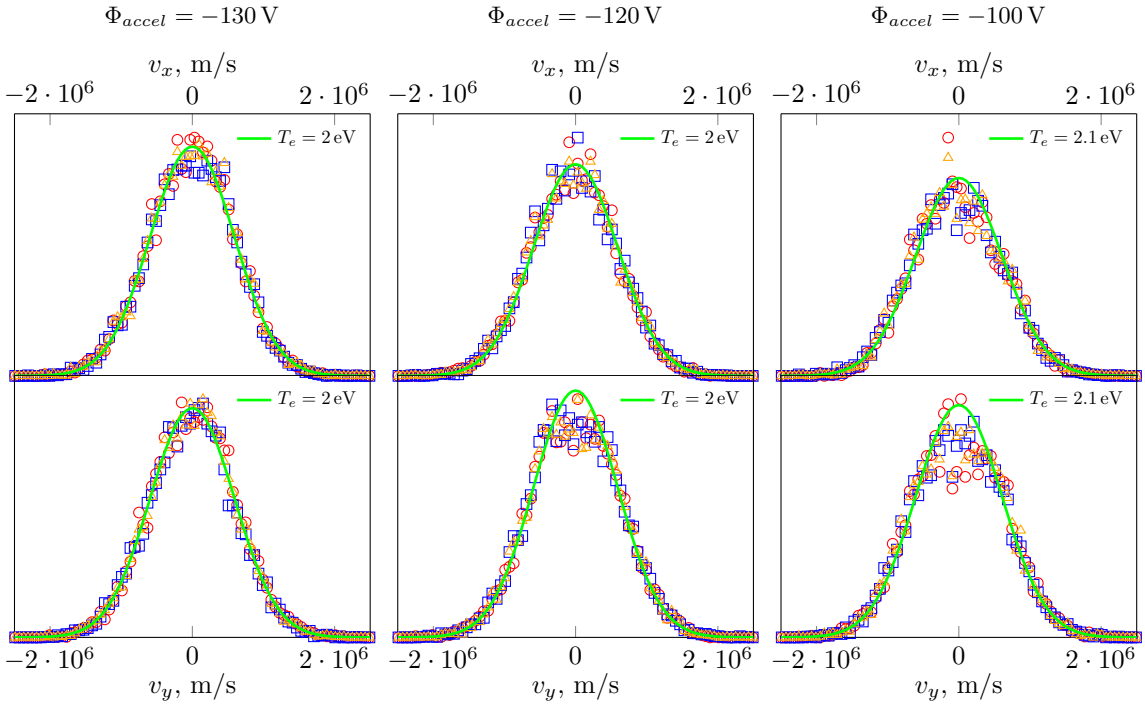

(b) $\Phi_{accel} = -130\,\mathrm{V}$ to $-100\,\mathrm{V}$.

Figure 12: VDF in beamlet axis at $x = 15\,\mathrm{mm}$ of infinite pattern for $\Phi_{accel} = -300\,\mathrm{V}$ to $-100\,\mathrm{V}$.

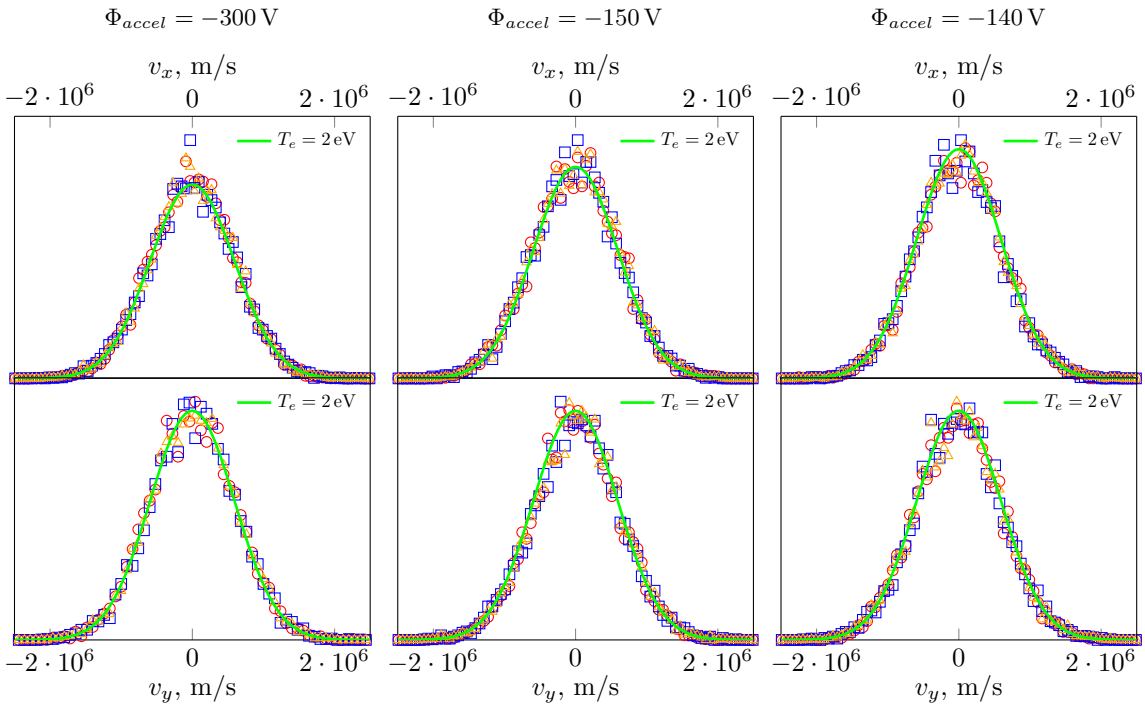

(a) $\Phi_{accel} = -300\,\mathrm{V}$ to $-140\,\mathrm{V}$.

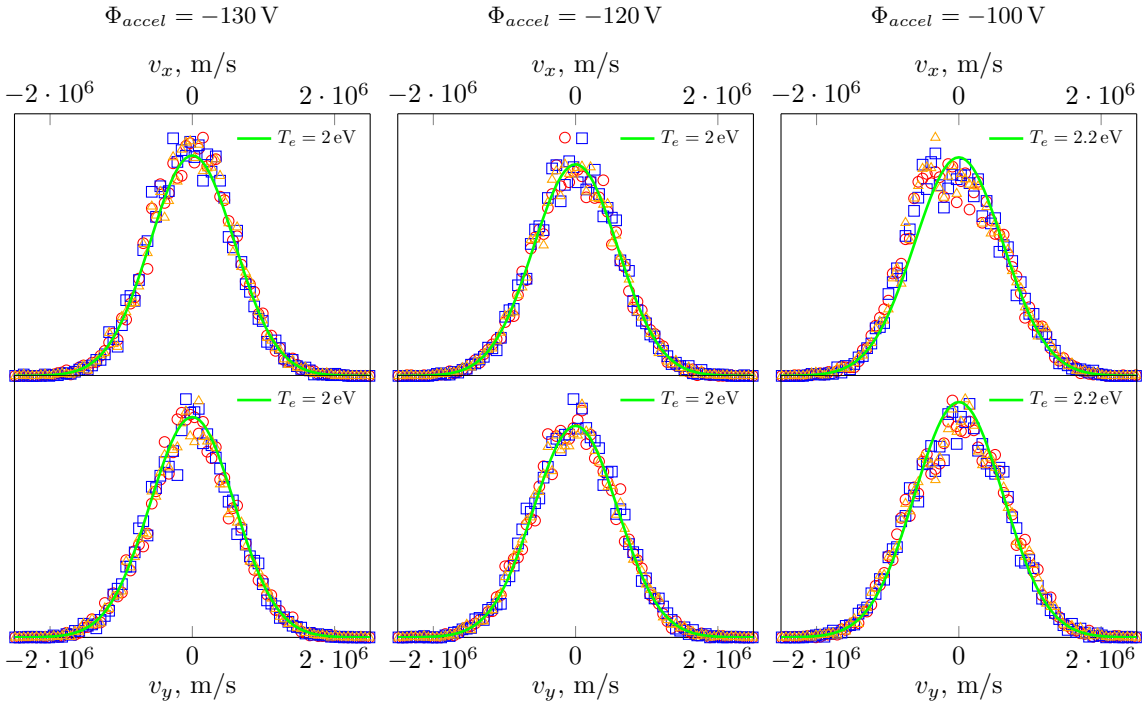

(b) $\Phi_{accel} = -130\,\mathrm{V}$ to $-100\,\mathrm{V}$.

Figure 13: VDF between beamlets at $x = 15\,\mathrm{mm}$ of infinite pattern for $\Phi_{accel} = -300\,\mathrm{V}$ to $-100\,\mathrm{V}$.

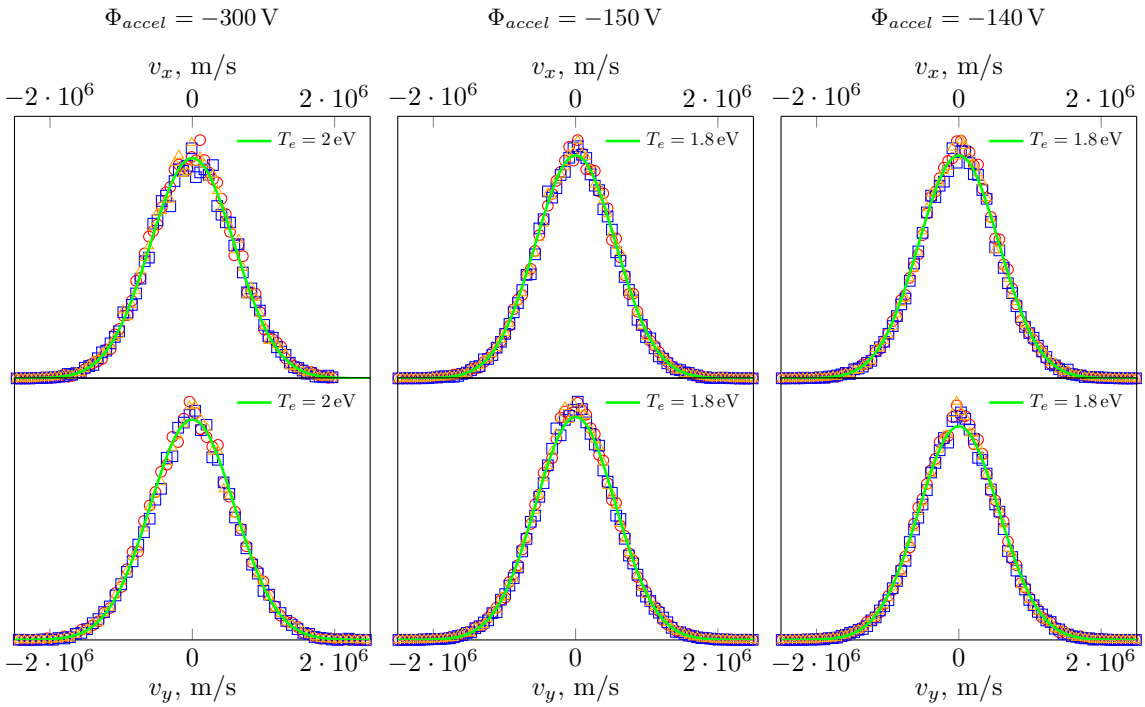

(a) $\Phi_{accel} = -300\,\mathrm{V}$ to $-140\,\mathrm{V}$.

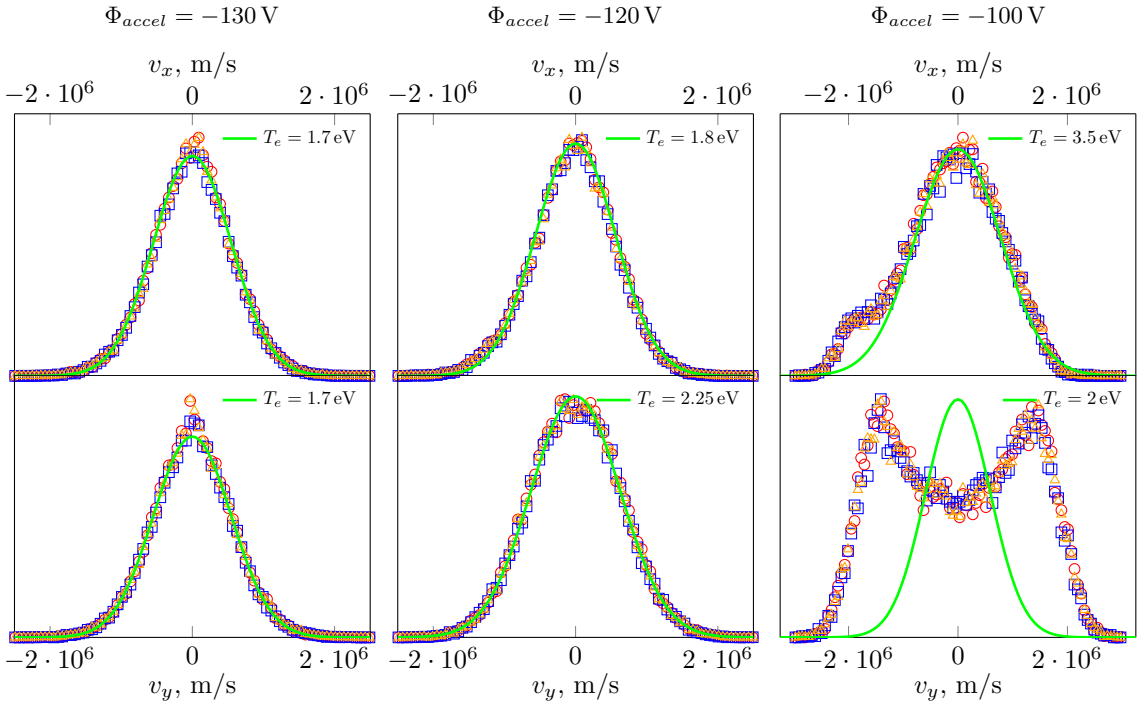

(b) $\Phi_{accel} = -130\,\mathrm{V}$ to $-100\,\mathrm{V}$.

Figure 14: VDF in beamlet axis at $x = 5\,\mathrm{mm}$ of infinite pattern for $\Phi_{accel} = -300\,\mathrm{V}$ to $-100\,\mathrm{V}$.

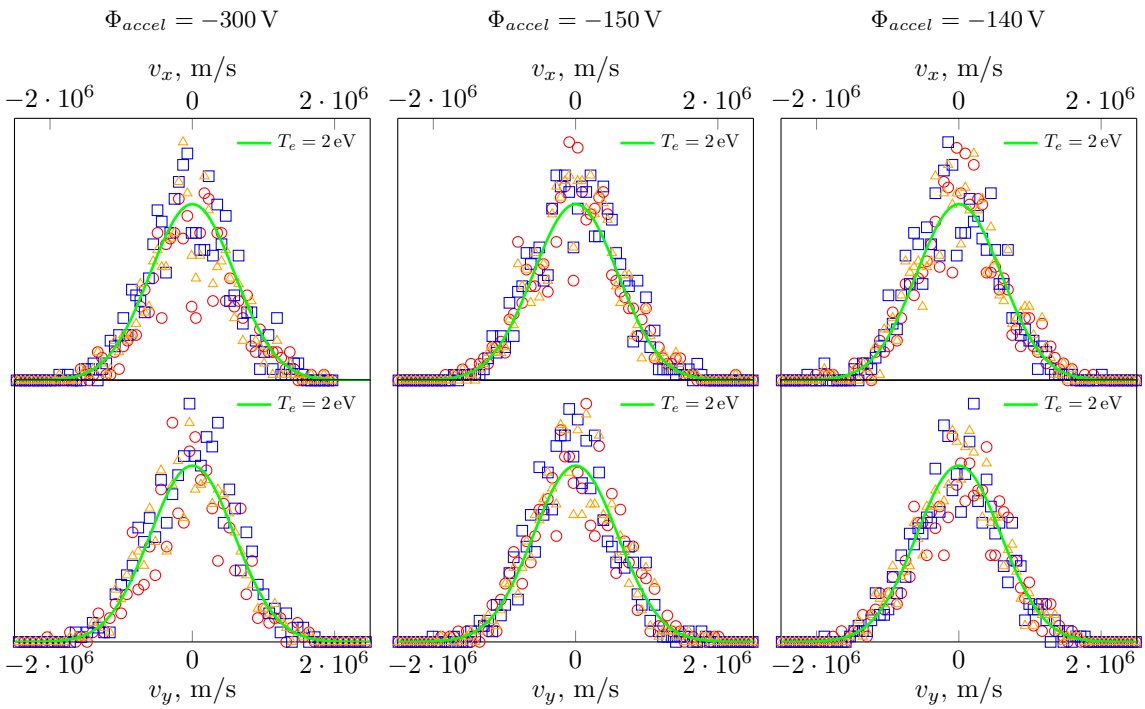

(a) $\Phi_{accel} = -300\,\mathrm{V}$ to $-140\,\mathrm{V}$.

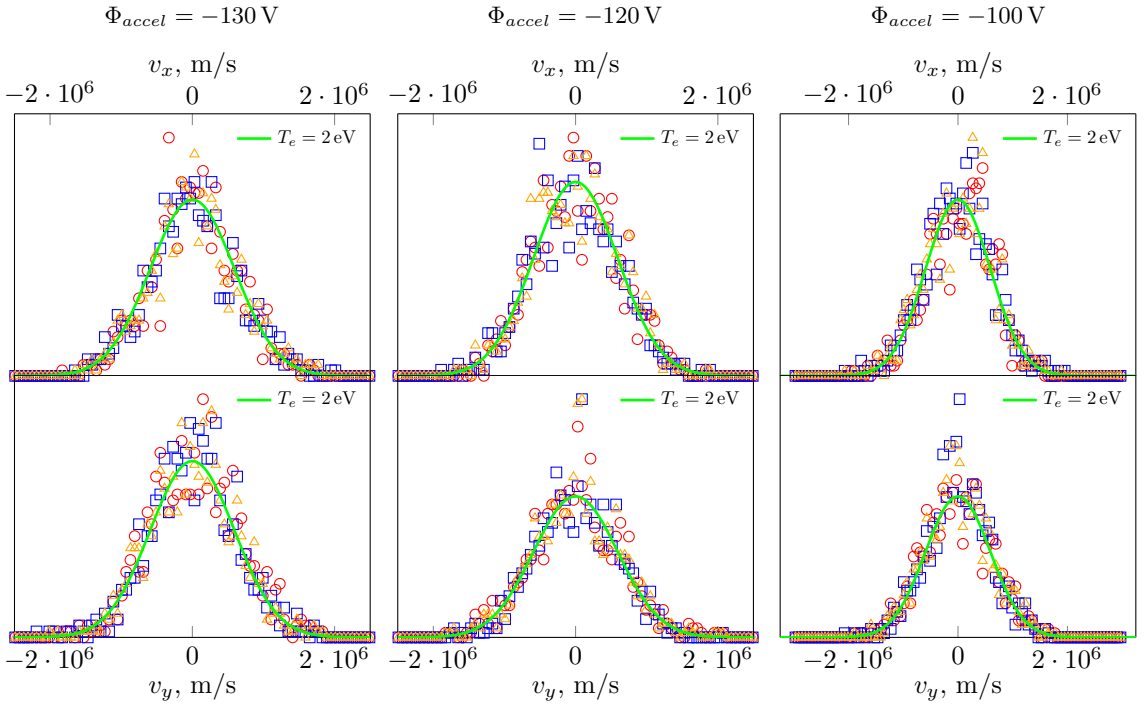

(b) $\Phi_{accel} = -130\,\mathrm{V}$ to $-100\,\mathrm{V}$.

Figure 15: VDF between beamlets at $x = 5\,\mathrm{mm}$ of infinite pattern for $\Phi_{accel} = -300\,\mathrm{V}$ to $-100\,\mathrm{V}$.

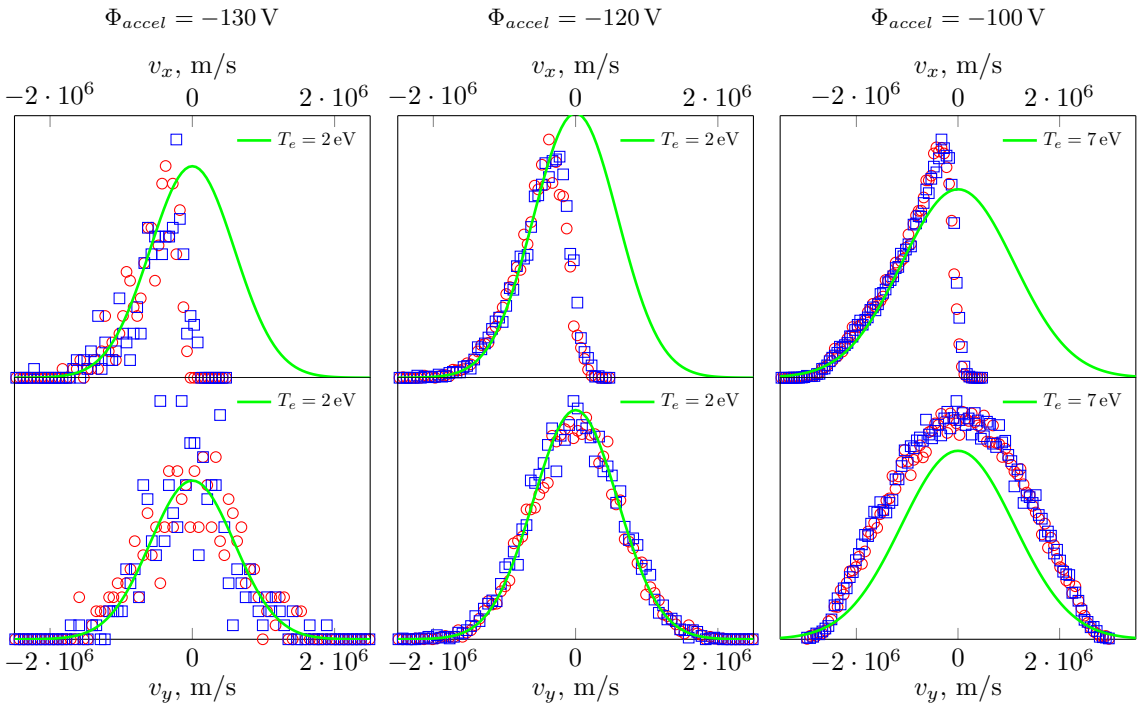

Figure 16: VDF in beamlet axis at $x = x_{\Phi,min}$ of infinite pattern for $\Phi_{accel} = -130\,\mathrm{V}$ to $-100\,\mathrm{V}$.

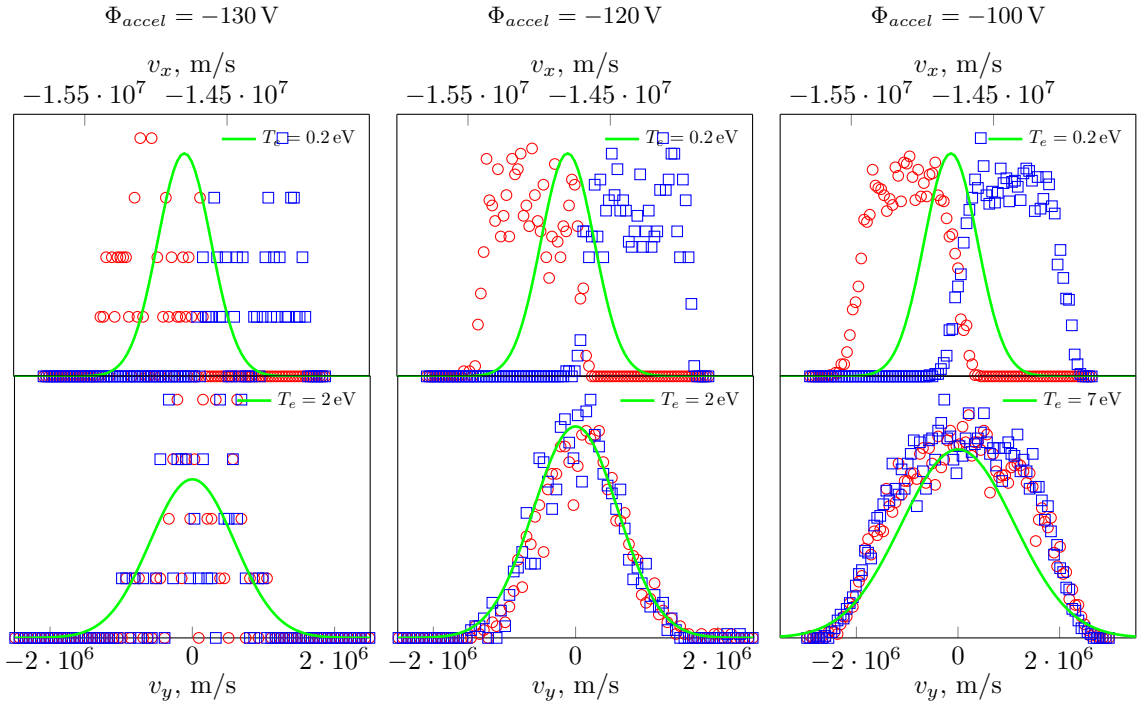

Figure 17: VDF in beamlet axis at $x = 0.55\,\mathrm{mm}$ of infinite pattern for $\Phi_{accel} = -130\,\mathrm{V}$ to $-100\,\mathrm{V}$.

Acknowledgments

We gratefully acknowledge Airbus and ArianeGroup GmbH for funding the main part of this work, as well as the Deutsche Forschungsgemeinschaft (DFG) for funding within the projects "Kinetic Algorithms for the Maxwell-Boltzmann System and the Simulation of Magnetospheric Propulsion Systems (No. FA 280/1-1)" and "Coupled PIC-DSMC-Simulation of Laser Driven Ablative Gas Expansions (SFB 716)". Computational resources have been provided by the Bundes-Höchstleistungsrechenzentrum Stuttgart (HLRS). Additionally, this work was partly performed on the computational resource ForHLR I funded by the Ministry of Science, Research and the Arts Baden-Württemberg and DFG. We thank Florian Hindelang and Marco Restelli for the help on implementing the Hybrid Discontinuous Galerkin method into PICLas.

References

[1]Boyd, I. D., "Simulation of Electric Propulsion Thrusters," *RTO-EN-AVT-194*, 2011.

[2]Nakano, M., Kajimura, Y., and Funaki, I., "JIEDI Tool: Numerical Life Qualification Tool for Ion Engine Optics," *ISTS 2011-b-29*, 2011.

[3]Farnell, C. C., Williams, J. D., and Wilbur, P. J., "Numerical Simulation of Ion Thruster Optics," *IEPC-03-073*, 2003.

[4]Turkoz, E., Sik, F., and Celik, M., "A Study of Ion Thruster Optics through Particle Simulations and Evaluation of the Near Plume Plasma Properties," *AIAA 2014-3412*, 2014.

[5]Wirz, R. E., Katz, I., Goebel, D. M., and Anderson, J. R., "Electron Backstreaming Determination for Ion Thrusters," *Journal of Propulsion and Power*, Vol. 27, No. 1, 2011, pp. 206–210.

[6]Munz, C.-D., Auweter-Kurtz, M., Fasoulas, S., Mirza, A., Ortwein, P., Pfeiffer, M., and Stindl, T., "Coupled Particle-In-Cell and Direct Simulation Monte Carlo method for simulating reactive plasma flows," *Comptes Rendus Mécanique*, Vol. 342, No. 10-11, 2014, pp. 662–670.

[7]Bin Baharudin, F., Miyasaka, T., Asato, K., Sugiyama, H., and Kobayashi, T., "Study on Electron Distributions in a Three Dimensional Particle Simulation of an Ion Engine," *Transactions of the Japan Society for Aeronautical and Space Sciences, ISTS-28*, Vol. 10, 2012.

[8]Birdsall, C. K. and Langdon, A. B., *Plasma Physics via Computer Simulation*, Hilger, Bristol, 1991.

[9]Bird, G. A., *Molecular Gas Dynamics and the Direct Simulation of Gas Flows*, Oxford University Press, Oxford, 1994.

[10]Birdsall, C. K., "Particle-in-cell charged-particle simulations, plus Monte Carlo collisions with neutral atoms, PIC-MCC," *IEEE Transactions on Plasma Science*, Vol. 19, No. 2, 1991, pp. 65–85.

[11]Boyd, I. D., "Review of Hall thruster plume modeling," *Journal of Spacecraft and Rockets*, Vol. 38, No. 3, 2001, pp. 381–387.

[12]Hindenlang, F., Gassner, G. J., Altmann, C., Beck, A., Staudenmaier, M., and Munz, C.-D., "Explicit discontinuous Galerkin methods for unsteady problems," *Comput. Fluids*, Vol. 61, may 2012, pp. 69–93.

[13]Cockburn, B., Dong, B., Guzmán, J., Restelli, M., and Sacco, R., "A hybridizable discontinuous Galerkin method for steady-state convection-diffusion-reaction problems," *SIAM Journal on Scientific Computing*, Vol. 31, No. 5, 2009, pp. 3827–3846.